Published in final edited form as:
J Mater Chem A Mater. 2018 May 16; 6: 9229–9236. doi:10.1021/acssuschemeng.8b01547.

Greener and size-specific synthesis of stable Fe-Cu oxides as earth-abundant adsorbents for malachite green

Ping Zhang[1], **Deyi Hou**[1,*], **Xuanru Li**[1], **Simo Pehkonen**[2], **Rajender S. Varma**[3], and **Xun Wang**[4]

[1]School of Environment, Tsinghua University, Beijing 100084, China [2]Department of Environmental and Biosciences, University of Eastern Finland, Kuopio, Finland [3]Water Resources Recovery Branch, Water Systems Division, National Risk Management Research Laboratory, US Environmental Protection Agency, Cincinnati, Ohio 45268, USA. [4]Department of Chemistry, Tsinghua University, Beijing 100084, China

Abstract

A greener and sustainable pathway to the assembly of Fe, Cu -based adsorbent is described using Virginia creeper (*Parthenocissus quinquefolia*) leaf extracts in presence of oxalic acid which avoids the use of toxic chemicals. Characterization of the synthesized mixed Fe, Cu oxides are carried out by SEM, TEM, XRD, FT-IR, XPS, and BET techniques; SEM and TEM results disclosed particle size ranging from 160 nm to 1 μm in presence of varying oxalic acid amounts of 0 and 0.1 mol/L. The X-ray photoelectron spectroscopy studies revealed that the sample comprised of Fe, Cu-based hybrid oxides and oxalates. The ensuing results from altered operational parameters namely initial pH, initial malachite green (MG) concentration, the sample dosage and the reaction temperature suggest that the MG adsorption capacity of synthesized materials could be well structured by simply varying the amount of oxalic acid. The optimal sample (S_3 sample) has a remarkably high maximum adsorptive capacity (~1399 mg/g) for aqueous MG removal at 303 K and natural pH (~ 6.58), which is superior to recently documented sorbents. The results demonstrate that the adsorption is spontaneous (i.e., $\Delta G < 0$) via an endothermic process wherein the synthesized adsorbent displayed excellent characteristics: 1) maintained a high adsorption capacity under a wide range of pH conditions; 2) remained chemically stable under ambient storage environments to allow for extended stowage; and 3) portrayed high reusability with no waning effect after 4 adsorption/desorption cycles.

Keywords

greener synthesis; Fe, Cu -based adsorbent; high adsorptive capacity; chemically stable

[*]Corresponding author: houdeyi@tsinghua.edu.cn.

1 Introduction

With the rapid pace of industrialization, contamination of air, water, soil, and groundwater has become a major challenge for modern societies [1–3]. Pollutants ranging from petroleum hydrocarbons to heavy metals require remediation efforts in order to protect the environment and human health [4–6]. Especially the discharge of colored wastewater from printing companies and pharmaceutical plants has inflicted immeasurable harm to the ecological environment and humans [7, 8]with more than 7×10^5 tons of dyes being released to the environment per annum [9, 10]. Consequently, it is urgent to explore economic and effective techniques for minimizing the dye contamination [11]. Research to date have shown that dye-laden effluents can be remediated by multiple approaches, including advance oxidation [12], membrane filtration [13, 14], adsorption [15, 16] and coagulation/flocculation [17], among others. Amongst these methods, adsorption has gained prominence in the decolourization of dye wastewater based on its simple design, easy operation and high efficiency [15, 18, 19].

Nanomaterials, as a representative of efficient adsorbents, have garnered attention due to their well-defined shape, large surface area, and easy-to-control porosities [20, 21]. To date, many smart nanomaterials including carbon nanotubes [22], graphene [23], and metal oxides [24] have been explored for the efficient removal of dyes. However, current studies show that the challenges remain for the mass production, primarily due to the complexity of the synthesis process and the use of hazardous reagents [25, 26]. On the other hand, environmental remediation activities can often result in secondary environmental impacts, such as energy and material consumption, air and water pollution during the manufacturing process, etc. [27–30]. In recent years, environmental professionals are increasingly interested in more sustainable means of environmental remediation [31–33]. Hence, it is imperative that greener, economic and efficient protocols for the preparation of nano-adsorbents need to be developed for application in dye removal.

Green nanotechnology predicates the development of novel and environmentally friendly method for the preparation of nanomaterials [34–36]. Considerable efforts have been expanded to adopt the phyto-synthesis methods for the rapid fabrication of nanomaterials, which are quick and devoid of secondary pollution thus ensuring the possibility of large-scale production of the nanomaterials [37–39]. The assembly of noble metal nanoparticles, such as Ag, Au, and Pt, using the plant biomass or extracts have been reported [36]; gold nanoparticle synthesis via plant extract-mediated preparation is comparable to that of chemical methods [40]. Previous studies have indicated that iron nanoparticles with different morphologies (e.g. spheres, platelets, and nanorods) could be obtained instantaneously in aqueous tea extracts [41–43]. In addition, metal oxide nanomaterials, such as iron oxide [37, 44], copper oxide [34, 45], manganese dioxide [46], zinc oxide [47], palladium oxide [48], could be synthesized using the extracts from tea, coffee, and sorghum. Interestingly, it has been found that the plant extracts, rich in polyphenols or related antioxidants, could serve as both reducing and capping agents [49, 50]. Interestingly, Makarov et al. [44] found that the iron nanoparticles synthesized by the plant extract with high concentrations of organic acids exhibited higher stability. Oxalic acid, a low molecular weight organic acid, is a metabolic product of organisms and is widely distributed in plants, animals, and fungi. To our

knowledge, the performance of oxalic acid in the assembly of nanomaterials has been largely overlooked [51], and such a study using this smallest dicarboxylic acid may provide necessary stimulation for researchers to develop an economic, safer and efficient adsorbent.

It is well known that the adsorptive properties of nanomaterials have a strong relation with their morphology and the surface area; samples with a higher surface area tend to have more adsorption sites. Nevertheless, the goal of obtaining materials with controlled size and morphology is still a challenging endeavour in the realm of green technology development. With this objective, an unprecedented attempt has been made here to fabricate Fe,Cu-based materials using leaf extract of Virginia creeper (*Parthenocissus quinquefolia*), and the effect of oxalic acid, as an additive, on the morphology of ensuing green synthesized hybrid oxides. Herein, we describe a simple, greener and inexpensive method for the assembly of hybrid oxides emanating from earth-abundant materials with the inherent advantage of wider flexibility in terms of controlling the morphology and their potential for broader applications. The prepared nanocomposites are tested for their potential for the removal of malachite green (MG) dye, and the optimal sample (S_3 sample) shows the maximum adsorption capacity of ~1399 mg/g at T of 303 K and at natural pH (~6.58), which is superior to most of the reported MG adsorption values. The optimized sample displays excellent stability and reusability in the removal of MG dye and we envisage that with aforementioned advantages the present greener synthetic route to the Fe, Cu-based adsorbent may have great potential for practical and sustainable textile dyeing wastewater treatment.

2 Experimental Materials and Methods

2.1 Chemicals and materials

All the used reagents, Ferric chloride hexahydrate ($FeCl_3 \cdot 6H_2O$), Cupric chloride dihydrate ($CuCl_2 \cdot 2H_2O$) were purchased from Beijing Chemical Reagents Company (China) and used directly without further purification.

2.2 Preparation methods

2.2.1 Preparation of Virginia creeper leaf extracts—Virginia creeper leaves (VC) were collected locally (from the Tsinghua University campus), washed with deionized water three times to eliminate surface dust, and dried at room temperature until their weight became constant under ambient conditions and then cut into pieces. The extract was prepared by boiling dry VC leaves in deionized water with a concentration of 60 g/L at 353 K for 90 minutes. Thereafter, the extracts were vacuum-filtered and stored at 277 K for further use.

2.2.2 Synthesis of the adsorbents—First, a specified quantity of oxalic acid ($C_{oxalic\ acid}$=0, 0.0125, 0.025, 0.05, 0.1 mol/L) was added to 200 mL extract of virginia creeper leaf under vigorous stirring. After stirring for 30 minutes, premixed 100 mL solution of $FeCl_3$ and $CuCl_2$ (0.12 mol/L) was added dropwise with vigorous stirring for 12 hours at ambient temperature. The formation of the adsorbent was indicated by the appearance of dark black precipitate. The sample was separated by centrifugation (4000 r/min for 10 minutes) and then washed with deionized water thrice. Finally, the product was dried for 12

hours at 333 K prior to its further use. The ensuing samples by varying the amount of oxalic acid at 0, 0.0125, 0.025, 0.05, and 0.1 mol/L, were labeled as S_1, S_2, S_3, S_4, and S_5, respectively.

2.3 Characterization

The morphology of all the samples obtained were examined using transmission electron microscopy (TEM, TECNAI G2). The Fourier transform infrared spectroscopy (FTIR, Nicolet IS10) was employed to identify the functional groups of the samples. The powder X-ray diffraction (XRD) patterns of the samples were acquired using a Rigaku D/Max-RB diffractometer with Cu/Kα radiation (k=0.15406 nm, 35 kV, 40 mA). X-ray photoelectron spectroscopy (XPS) measurements were performed on a Thermo Fisher Escalab 250Xi Spectrometer with a monochromated Al K excitation, which was used to determine the surface chemical elemental composition and its chemical changes. The Brunauer–Emmett–Teller (BET) specific surface area and the pore size distributions were analysed by nitrogen adsorption–desorption measurements via an Autosorb-1 specific surface area analyser (Quantachrome Instruments, USA).

2.4 Adsorption experiments

The MG adsorption capacity of the prepared samples was investigated by a series of batch experiments. Some experimental parameters, such as adsorbent dosage, solution pH, contact time, initial concentration and temperature, were taken into consideration. For a typical adsorption test, a certain dose (0.3 g/L) of sample was added to 20 mLs of a 50 mg/L MG aqueous solutions at 303 K, After shaking for 12 hours until an adsorption equilibrium was reached, the mixture was separated by centrifugation (4000 r/min for 5 minutes). The effect of dosage was investigated by changing the added amount of the sample (0.05–0.7 g/L) at natural pH of circa 6.6; pH values could be adjusted using HCl or NaOH solutions. The concentrations of the MG solution were in the range of 50 to 500 mg/L. The batch adsorption experiments focusing on the effect of temperature on the adsorption capacity were carried at 303, 313, and 323 K, respectively. Finally, the concentration of MG in the supernatant was measured by a UV–Vis spectrophotometer (Shimadzu UV-1800 spectrophotometer, Japan) at a wavelength of 619 nm. The equilibrium adsorption capacity Q_e (mg/g) and the removal efficiency of MG were determined by the following equations:

$$Q_e = \frac{(C_0 - C_e)V}{m} \quad 1$$

$$\text{Removal efficiency}(\%) = \frac{100(C_0 - C_e)}{C_0} \quad 2$$

where C_0 (mg/L) and C_e (mg/L) are the MG concentrations in the solution at t_0 and t_e. The time(t_e) required to reach the equilibrium could be determined by Fig. S2, and the adsorption

time(12 h) in the test of adsorption equilibrium capacity Q_e was set longer than t_e. V (L) is the total volume of the suspension, and m (g) is the mass of the adsorbent.

2.5 Desorption and regeneration of adsorbent

The experimental regeneration of the adsorbent was carried out in the four successive cycles. In each cycle, 6 mg of the adsorbent was added into 20 mLs of a 50 mg/L MG solution followed by shaking for 12 hours (303 K). Then, the MG-loaded adsorbent was obtained through centrifugation and washing with anhydrous ethanol several times until no green color was evident. Finally, the regenerative adsorbent was placed in an oven at 343 K overnight, and then utilized for the next adsorption-desorption cycle. The adsorption capacity of the regenerated sample was calculated by the aforementioned method.

3 Results and discussion

3.1 Characterization of samples

To unravel the distribution of elements on the surface of the adsorbent samples and their valence states, the XPS measurements were carried out and the spectra are shown in Figure 2. As displayed in Fig 2 A, the peaks of the XPS full spectra indicated that C, O, and Fe were the predominant elements in S_1-S_5 samples. The peak for the copper element was not obvious in the S_1-S_4 samples due to its low content or its high dispersibility. Fig. 2 B presents the fitting curves of C 1s peaks in the S_1, S_3, and S_5 samples; the peaks are obviously different from samples prepared by chemical method [51]. The three peaks located at binding energies of 284.6, 286.7, and 289.1 eV can be assigned to the C-H(C-C, C=C), C-O, and O=C-OH functional groups[7, 61], respectively. The presence of multiple C peaks implies that some biomolecules are attached to the surface of the adsorbent samples [62]. In Fig. 2 C, the two peaks located at 531.6 and 532.8 eV suggested the presence of the lattice oxide oxygen in the metal oxides (Fe-O/Cu-O) of samples [63] and O=C-OH/C-OH functional groups [64], respectively. For S_1 sample without oxalic acid, the C and O peaks may be ascribed to polyphenols, sugars, or other related phytochemicals present in the virginia creeper leaf extract [64]. Similar results have been obtained for materials by Wang et al.[65, 66], and they were classified as iron complex nanoparticles. Moreover, combined with the characteristics of Fig. 2 B and 2 C, one can see that, with the increasing addition of oxalic acid, the intensity of the peaks located at 289.1 and 532.8 eV has increased, indicating the enrichment of O=C-OH functional groups on the surface of the adsorbent samples [67]. Figure 2 D shows the spectra of Fe and Cu in sample S_3. The Fe 2p3/2 and Fe 2p1/2 core levels are located at 711.3 and 725.0 eV, respectively, which are consistent with those reported for iron oxide previously [51, 64, 68]. The two main peaks located at 935.3 and 953.7 eV belong to Cu2+ in CuO [51]. Based on these results, it can be concluded that a process of enrichment of carboxylate groups on the surface of iron and copper hybrid oxides occurs with the oxalic acid addition ranging from 0 to 0.1 mol/L. Furthermore, these results also provide strong evidence for the shell being mainly composed of biomolecules, metal oxides and oxalate on their surfaces.

The XRD pattern of the S_1-S_5 samples in the 2θ range of 2–80° is shown in Fig. 3. In this analysis, no obvious peaks for the S_1-S_3 samples were observed, indicating that the greener

protocol produced amorphous iron-copper oxides, which was similar to the previously published data on synthetic nanoparticles using tea and eucalyptus extractives [69]. Furthermore, with the addition of the oxalate at more than 0.05 mol/L during the synthesis, the XRD pattern of S_4 and S_5 samples showed diffraction patterns at 2θ values of 22.9, 36.2, 36.9, 42.4, 46.8, and 52.1° corresponding to the [110], [120], [210], [111], [220], and [130] planes of the orthorhombic $CuC_2O_4 \cdot nH_2O$ lattice, respectively. This obviously indicated the existence of oxalate in the S_4 and S_5 samples, which is consistent with the results of XPS spectra.

The FT-IR measurement was employed to gain detailed information regarding the surface group of the green synthetic samples. As shown in Fig. 4 A, the characteristic peaks of all samples at around 3436.7 cm−1 could be pertinent to O-H stretching vibration due to the water present on the surfaces of the samples [70, 71]. The absorption bands located at 1614 cm−1 correspond to the C=C aromatic ring stretching vibration, which may be related to polyphenols or sugars/glycosides in plant extracts [62, 72]. The peaks at 1461 cm−1 are attributed to the O–H bending of the phenolic group [73]. The absorption band at around 1069 cm−1 is ascribed to the C=O of carboxylic acid whereas bands at around 546 cm−1 refer to metal-oxygen stretch in metal oxides [74]. All of the above peaks revealed that the basic bonding types of all samples were practically similar. Moreover, the peaks for S_4 and S_5 samples at 1320 and 820 cm−1 are assigned to the C-O and C-C stretching vibrations of coordinated oxalic acid; the presence of oxalate was also confirmed from the corresponding peaks at 1412 cm−1 for oxalate coordination [51]. Moreover, the corresponding peak intensity of the S_5 sample is higher than that of S_4, indicating surface enrichment of the carboxylate group. This is consistent with the conclusions of the adsorbent characterization via XPS and XRD.

The FTIR spectrum of the S_3 sample before and after MG adsorption on the S_3 sample are depicted in Fig. 4 B. The peak at 1069 cm−1 decreased on MG-adsorbed sample and this could be pertinent to electrostatic interactions between the –COO- group of the S_3 sample and the positively charged nitrogen centre of the MG dye [75, 76]. The appearance of a new peak at 1237 cm−1 indicated that a certain number of MG molecules were adsorbed on the surface of the adsorbent material [53, 75]. In addition, the peak at 1461 cm−1 in the S_3 sample shifted relatively to lower wavenumbers and its intensity decreased after MG adsorption, revealing that the interactions could take place between the –OH groups and the MG dye molecules [75]. Based on the above analysis, it can be deduced that the MG adsorption process materialized via electrostatic interactions.

TEM, SEM—The TEM images of samples without (S_1 sample) or with the oxalic acid (S_2, S_3, S_4, and S_5 samples) are shown in Fig. 5. It can be observed that the samples obtained by the greener process consist of particles with diameters ranging from 160 nm to 1 μm. Interestingly, the particles with a diameter of about 400 nm were present in the S_1 sample, after the addition of oxalic acid in the protocol, whereas the diameter of the ensued S_2 sample decreased to 160 nm. However, as the amount of oxalic acid was further increased to 0.1 mol/L, the diameters of the prepared sample (S_5 sample) increased to 1 μm. It is well known that the adsorption capacity of any adsorbent has a very strong correlation with their surface active sites; smaller the particle size of the adsorbent, the larger the surface area they

possess as more active sites are available. Combined with the results of TEM images, the diameters of the prepared samples can be adjusted and controlled in the range from ~ 160 nm to ~ 1 μm, which is beneficial for the alteration of the adsorption capacity of MG. The SEM image of S_3 sample and its corresponding elemental mapping are shown in Figure S1; green, blue and red images indicate the O-, Fe- and Cu-enriched areas of the sample, which implied that the elements are well dispersed on the surface of the S_3 sample. In conjunction with the results of XPS and XRD, it is obvious that this greener synthetic method of material preparation need to be studied due to its simplicity and the utilization of low-cost earth-abundant raw materials.

The Brunauer-Emmett-Teller (BET) specific surface area and pore size distribution of S_1, S_3, and S_5 samples were obtained next via N_2 adsorption-desorption measurements at 77 K. According to Figure 6 A, the type-Ⅳ behaviour with a hysteresis loop is observed, and this was ascribed to capillary condensation. This phenomenon indicates the existence of mesopores in the samples [28]. The Brunauer −Emmett − Teller (BET) surface areas increased from 13.664 $m2 \cdot g{-}1$ for S_1 sample to 19.214 $m2 \cdot g{-}1$ for S_3 sample, and then reduced to 13.084 $m2 \cdot g{-}1$ for S_5 sample, which affirmed the important role of the oxalic acid in the synthesis. Generally, the higher surface area can provide more active sites and provide sufficient interaction between the adsorbents and the dye molecules [77]. The distribution of pore sizes (Fig. 6 B) in the range of 2.1–4.0 nm further confirmed the existence of mesopores on the surface of the adsorbents. These results indicate that both, the presence of oxalic acid and its amount used significantly impact on the textural properties of the prepared samples.

3.2 Effects of operating conditions on MG adsorption

3.2.1 Effects of the addition of oxalate on MG removal and adsorption kinetics—

In the process of pollutant removal, the removal efficiency of adsorbents is closely related to their composition. Firstly, the MG adsorption capacity of Fe alone without oxalic acid and Fe, Cu-based material without oxalic acid were investigated (natural pH, temperature 303 K, 20 mL 50 mg/L MG solution, dosage 0.3 g/L) and the results indicated that the values of latter(Q_e: 110.15 mg/g) was better than that of former (Q_e: 32.69 mg/g). In order to further enhance their performance in environmental remediation, the effect of oxalate on the adsorption capacity of MG was investigated. As is observed in Fig. S2A, the MG adsorption capacity of all samples initially increased rapidly, and then became constant. The fast adsorption phase may be attributed to the high concentration gradient and numerous surface sites, which benefited the transfer and adsorption of the MG molecule. Then the effect of these favourable adsorption factors would decline with an increase in contact time, thereby resulting in the slower adsorption rate [78]. Moreover, the S_3 and S_4 samples reached the adsorption equilibrium in the first 30 minutes of contact time; adsorption capacity constants of these samples being in the order: S_2 (167.02 mg/g) > S_3 (166.57 mg/g) > S_4 (164.86 mg/g) > S_1 (110.15 mg/g) > S_5 (37.48 mg/g). Combined with the results of the XPS, FTIR and BET analysis, the high capacity of S_2-S_4 samples may be attributed to their size, high surface area and their oxalate-enriched surface, which could provide more active sites and electrostatic attraction for MG dye molecules. Considering the cost, the removal

rate and the efficiency of the adsorbent, the S_3 sample was selected as the main research candidate for further experiments.

Later, to understand the essence of the adsorption process, the pseudo-first-order kinetics model, pseudo-second-order kinetics model, and intraparticle diffusion model were adopted to analyse the adsorption kinetics [8, 78, 79]. These models can be expressed as follows:

$$\ln(q_e - q_t) = \ln q_e - k_1 t \quad 3$$

$$t/q_t = 1/(k_2 q_e^2) + t/q_e \quad 4$$

$$q_t = k_{pi} t^{1/2} + C_i \quad 5$$

where q_e and q_t (mg/g) are the amounts of MG dye adsorbed at equilibrium and given time, respectively. k_1 (min−1), k_2 (g/mg/min) and k_{pi} (mg g−1 min−0.5) represent the rate constants of pseudo-first-order, pseudo-second-order, and intraparticle diffusion model, respectively. C_i is a constant (mol/g), which can be used to determine whether the controlling step is intraparticle diffusion [52]. If the q_t is linear with t1/2 and the value of C_i is zero, the adsorption process is controlled by the intraparticle diffusion only; if the results of curve fitting contain multi-line plots, then there exists two or more steps in the adsorption process [52]. The line plots and the corresponding kinetic parameters of the models are shown in Fig. S2 and Table 2.

By contrasting the correlation coefficient of the different models, it was found that the adsorption of MG onto samples fitted well with the pseudo-second-order model with higher R2 values (> 0.99) than with the pseudo-first-order kinetics model (R2 < 0.99). The equilibrium adsorption capacity values calculated from the pseudo-second-order model are close to the experimental values, indicating that the pseudo-second-order kinetic model is more suitable for describing the adsorption process of MG onto the adsorbent samples [53, 80]. Additionally, it can be noted from Fig. S2D that the plots were non-linear over the entire time, and the values of intercepts were not zero, suggesting that the dye adsorption process was controlled by multiple processes [52].

3.2.2 Effects of solution pH—The pH value is an important factor affecting the adsorption process, because it influences the surface charge and the ionic state of the adsorbent. Therefore, the effects of initial pH on the MG removal were investigated. As illustrated in Fig. 7, the MG adsorption capacity of S_3 sample increased gradually with the solution pH range from 3.13 to 9.23; similar phenomenon has been reported for the adsorption of MG on activated carbons and rattan sawdust [56]. MG is a cationic dye and the high concentration of H+ at lower pH values may compete with dye cations for the available adsorption sites of the sample, thus a lower adsorption capacity was observed [59]. In

addition, the carboxylate groups on the surface of the adsorbent sample can be transformed to –COOH groups at lower pH values (pH < 4.70) [57], which is unfavourable for the interaction between the MG dye molecule and the S_3 sample, thus leading to a decrease in MG adsorption capacity. In contrast, at higher pH values, the surface of sample became negatively charged and exhibited a high MG adsorption capacity. In summary, the as-prepared sample showed a high adsorption capacity over a wide pH range, indicating its promising and excellent adsorption performance in the field of dye wastewater remediation.

3.2.3 Effect of adsorbent dose—The relationship between the dosage and the MG adsorption capacity of samples was investigated next. Different amounts of adsorbent (0.05–0.7 g/L) were added to 20 mLs of the dye solution with an initial MG dye concentration of 50 mg L−1, and then shaken at 303 K, natural pH of circa 6.6 for 12 hours. As shown in Fig. 8, with the increase of dosage, the MG removal efficiency of sample increased rapidly, while the equilibrium adsorption capacity of the sample decreased. The improvement in the removal efficiency can be attributed to the enhanced surface area and the more available active surface sites [81]. Additionally, the decreased adsorption capacity at high dosages is due to the reduced amount of MG molecules adsorbed per unit mass of the adsorbent, thus causing the decrease in Q_e values with increasing adsorbent mass concentrations [81].

3.2.4 Effect of initial concentration, temperature and adsorption isotherms—The effect of initial MG concentration (from 50 to 500mg/L) and temperature (from 303 to 323 K) on the adsorption capacity of the S_3 sample was carried out. As shown in Fig. S3, the adsorption capacity of the adsorbent sample increased with the increase of MG concentration when the temperature was kept constant. This may be explained by the strong driving force, which exists in the solution with a high concentration gradient, thus benefitting the transfer of the dye molecules between the solid phase and the liquid phase, and causing more dye molecules to be adsorbed. Besides, it is clearly observed that the adsorption capacity showed the incremental trend at high temperatures, implying that the process of adsorbing MG molecules was endothermic in nature.

To better illustrate the adsorption behaviour between the adsorbate and the adsorbent in the solution, the Langmuir, Freundlich, and Dubinin-Radushkevish (D-R) isotherm models were used to describe the adsorption processes[82]. The Langmuir isotherm model is based on the hypothetical premise that monolayer adsorption occurs at the specific homogeneous sites within the adsorbent [61]. The Freundlich adsorption isotherm model is founded on the assumption that the interactive behavior is related to multiple-layer adsorption occurring on the heterogeneous surface with different adsorption energies and affinities [61]. The Dubinin-Radushkevish (D-R) isotherm model is usually adopted to distinguish whether the adsorption is physical or chemical [83]. The three model equations can be described as follows:

$$C_e/q_e = 1/(q_m K_L) + C_e/q_m \quad 6$$

$$\ln q_e = \ln K_F + \frac{1}{n} \ln C_e \quad 7$$

$$\ln q_e = ln q_m - k\varepsilon^2 \quad 8$$

where C_e is the equilibrium concentration of MG (mg L− 1), q_e is the quantity of MG adsorbed per gram of sample after equilibrium (mg g− 1), q_m represents the maximum adsorption capacity (mg g− 1), K_L is the Langmuir adsorption constant (L mg− 1), K_F and 1/n are the proper constants of the Freundlich isotherm, which are respectively represented by the adsorption capacity and adsorption intensity [61]. Finally, k (mol2·kJ− 2) is the D-R isotherm constant ($E = \frac{1}{\sqrt{2k}}$, when E < 8 kJ mol−1, it is physisorption and if it is between 8–16 kJ mol−1, it is chemical in nature), and ε represents Polanyi potential ($\varepsilon = RT\ln(1+1/C_e)$).

The isotherm parameters of each model are summarized in Table 3. It has been observed that the correlation coefficient (R2>0.99) of the Langmuir model was higher than that of the Freundlich (R2:0.857–0.935) and the D-R model (R2:0.738–0.914), and this verified that the MG adsorption behavior of the S_3 sample could be better expressed by the Langmuir equation. Moreover, it was found that the maximum adsorption capacity of sample increased from 1399 to 1977 mg/g when the temperature increased from 303 to 323 K, which was higher than adsorbents previously reported (Table 1). In addition, the values of 1/n obtained from the Freundlich model are smaller than 1, suggesting that the removal condition is favourable for the adsorption reaction. In the D-R model, the values of free adsorption energy (E = (2k)− 0.5) were lower than 8 kJ/mol, thus the physical adsorption process played the main role in the adsorption of MG onto the S_3 sample.

Besides, the Langmuir isotherm is also expressed in terms of a dimensionless constant called a separation factor (R_L), which is defined by Eq. 9:

$$R_L = 1/\left(1 + K_L C_0\right) \quad 9$$

where C_0 (mg L− 1) is the initial MG concentration. The R_L value indicates the isotherm is favourable ($0 < R_L < 1$), unfavorable ($R_L > 1$), linear ($R_L = 1$), or irreversible ($R_L = 0$) [79]. In this study, the calculated R_L values are between 0 and 1, indicating that the adsorption of MG on the S_3 sample is favourable [79].

3.2.5 Adsorption thermodynamics—Thermodynamic parameters, such as the Gibbs free energy (ΔG), the enthalpy changes (ΔH), and the entropy change (ΔS), can provide further information about the inherent energetic changes and feasibility of the adsorption reaction. The values of ΔG, ΔH and ΔS can be obtained by the following equations:

$$K_d = \frac{q_e}{C_e} \quad 10$$

$$\Delta G_0 = \Delta H_0 - \mathrm{T}\Delta S_0 \quad 11$$

$$\ln K_d = -\Delta H_0/(RT) + \Delta S_0/R \quad 12$$

where K_d is the equilibrium constant (mL/g), q_e is the adsorption capacity (mg/g), and C_e is the MG concentration at equilibrium(mg/L). R is the universal gas constant (8.314 J / (mol·K)) and T is the absolute temperature (K). The thermodynamic parameters ΔH and ΔS can be obtained from the slope and the intercept of the linear plot of ln K_d vs. 1/T and are given in Fig. S4 and Table 4. The positive and a smaller value of ΔH (less than 40 kJ mol−1) for the adsorbent indicates that the adsorption process is endothermic and governed by physical adsorption [52, 81], respectively. This is consistent with the earlier conclusion that the higher temperature improved the adsorption capacity. The positive value of ΔS indicated a randomness enhancement in the process of adsorption [81]. The negative ΔG values (−10.647 to −13.026 kJ/mol) established that the MG adsorption process was feasible and spontaneous [81]. Besides, the ΔG values decreased with the increase of temperature, indicating the enhanced feasibility of the adsorption via physical forces [52]. Thus, higher temperatures were favourable to the adsorption of MG, which is in good agreement with the adsorption isotherms.

4 Reusability

In addition to the adsorption rate and adsorption capacity, the reusability of adsorbent is of paramount importance, an important consideration to evaluate the value of adsorbent's practical applications. To date, the main eluents and processes used for the desorption of adsorbent comprise acids (HCl, HNO_3), bases (NaOH, $NaHCO_3$), organic solvents (ethanol, methanol, and acetone), ultrasound, and thermal regeneration [84, 85]. Usually, the ultrasound and thermal regeneration methods are limited in view of the expensive nature of devices. Compared with acids and bases, the low toxicity and low corrosivity of ethanol have certain advantages. In this study, anhydrous ethanol was selected as the desorbing agent and the adsorption-desorption experiment was conducted by adding the S_3 sample (0.3 g/L) to the MG solution (50 mg/L), then shaken oscillatively to adsorption equilibrium. Four cycles of adsorption–desorption were completed and the results are shown in Fig. 9. The adsorption capacity of the reused adsorbent remained at almost 162.78 mg/g for the four cycles, indicating that anhydrous ethanol can be regarded as a good desorption agent and the absorbent has a good recyclable performance thus rendering it a potentially effective adsorbent for the removal of MG.

5 Stability

The stability of S_3 sample was evaluated by adding fresh (1 day) and aged (stored in air for 3, 5, 7, 14, 21 and 28 days) S_3 sample (0.3 g/L) to MG solution (50 mg/L), and then oscillating it to adsorption equilibrium (see Fig. 10); adsorption capacity remained consistent at ~ 162 mg/g, suggesting that the sample was highly stable. Earlier studies involving similar preparations with extracts corroborates the stabilizing aspects. Prasad et al. [86] prepared the iron oxide nanocrystals using Garlic Vine leaf extract, with the premise that the adhering organic biomolecule on the nanoparticles surface serve as steric stabilizer against their inherent agglomeration behavior, a typical trait of small particles. Makarov et al. [44] compared the amorphous iron oxide nanoparticles produced by *Rumex acetosa* extracts which were more stable than that produced by *Hordeum vulgare* extracts; the presence of organic acids (such oxalic or citric acids) presumably stabilized the iron nanoparticles. In the context of our work, the high stability of the S_3 sample may be related to the existence of the biomolecules and oxalate on the surface. Moreover, the high stability of this sample to air not only saves the storage cost of the adsorbent, but also bodes well for the potential applications in real world remediation scenarios involving transportation.

6 Conclusions

There is a growing need in the environmental remediation field which calls for greener remediation reagents deployed under more sustainable means [87–89]. In the present study, a green, ecofriendly method, devoid of hazardous materials (e.g. toxic reductants such as borohydrides or hydrazine, and solvents), was designed for the economical and efficient synthesis of Fe, Cu-based adsorbents. XPS analysis showed that the green synthetic material was mainly composed of Fe, Cu-based hybrid oxides and oxalic acid; the electronic attraction between the material and MG dye molecules being responsible for the adsorption process. In the dye removal test, the samples comprising an appropriate amount of oxalate exhibited an enhanced adsorption ability for MG dye, and the adsorption capacity was only slightly influenced by solution pH. Moreover, it is worth noting that the MG adsorption process followed the pseudo-second-order kinetic model and Langmuir adsorption isothermal model; maximum MG adsorption capacity of the selected sample (S_3) was calculated to be 1399 mg/g at near neutral pH (~6.58) and 303 K, which is higher than that of most recently reported adsorbents. In addition, the S_3 sample exhibited high stability and good reusability, which are important attributes for practical application. With these findings, this work not only promotes the use of natural, earth-abundant and renewable resources in synthesizing novel and efficient absorbents, but also provide a simple, convenient and cost-effective strategy for the purification of dye wastewater. This study may stimulate researchers to explore applications of this sustainable strategy for the remediation of other pollutants.

Supplementary Material

Refer to Web version on PubMed Central for supplementary material.

Acknowledgments

This work was supported by China's National Water Pollution Control and Treatment Science and Technology Major Project (Grant No. 2018ZX07109–003), the Thousand Talents Program of the Chinese government and Tsinghua University.

References

[1]. Hou D, Leu R-J, Optimizing the remedial process at a petroleum hydrocarbon contaminated site using a three-tier approach, Journal of Environmental Engineering 135 (2009) 1171–1180.

[2]. Hou D, Vision 2020: More Needed in Materials Reuse and Recycling to Avoid Land Contamination, Environmental Science & Technology 45 (2011) 6227–6228. [PubMed: 21740008]

[3]. Qi S, Hou D, Luo J, Optimization of groundwater sampling approach under various hydrogeological conditions using a numerical simulation model, Journal of Hydrology 552 (2017) 505–515.

[4]. Hou D, Li F, Complexities Surrounding China's Soil Action Plan, Land Degradation & Development 28 (2017) 2315–2320.

[5]. Hou D, O'Connor D, Nathanail P, Tian L, Ma Y, Integrated GIS and multivariate statistical analysis for regional scale assessment of heavy metal soil contamination: A critical review, Environmental Pollution 231 (2017) 1188–1200. [PubMed: 28939126]

[6]. Chen MM, Wei D, Chu W, Wang T, Tong DG, One-pot synthesis of O-doped BN nanosheets as a capacitive deionization electrode for efficient removal of heavy metal ions from water, J. Mater. Chem. A 5 (2017) 17029–17039.

[7]. Zhu Z, Wu P, Liu G, He X, Qi B, Zeng G, Wang W, Sun Y, Cui F, Ultrahigh adsorption capacity of anionic dyes with sharp selectivity through the cationic charged hybrid nanofibrous membranes, Chemical Engineering Journal 313 (2017) 957–966.

[8]. Chen MM, Wei D, Chu W, Hou LP, Tong DG, Novel mesoporous amorphous B–N–O–H nanofoam as an electrode for capacitive dye removal from water, J. Mater. Chem. A 5 (2017) 21400–21413.

[9]. Wang J, Qin L, Lin J, Zhu J, Zhang Y, Liu J, Van der Bruggen B, Enzymatic construction of antibacterial ultrathin membranes for dyes removal, Chemical Engineering Journal 323 (2017) 56–63.

[10]. Santhosh C, Daneshvar E, Kollu P, Peräniemi S, Grace AN, Bhatnagar A, Magnetic SiO 2 @CoFe 2 O 4 nanoparticles decorated on graphene oxide as efficient adsorbents for the removal of anionic pollutants from water, Chemical Engineering Journal 322 (2017) 472–487.

[11]. Zhang P, Lo I, O'Connor D, Pehkonen S, Cheng H, Hou D, High efficiency removal of methylene blue using SDS surface-modified ZnFe2O4 nanoparticles, Journal of Colloid and Interface Science 508 (2017) 39–48. [PubMed: 28818655]

[12]. Liu ML, Chen BB, Li RS, Li CM, Zou HY, Huang CZ, Dendritic CuSe with Hierarchical Side-Branches: Synthesis, Efficient Adsorption, and Enhanced Photocatalytic Activities under Daylight, ACS Sustainable Chemistry & Engineering 5 (2017) 4154–4160.

[13]. Li Q, Li Y, Ma X, Du Q, Sui K, Wang D, Wang C, Li H, Xia Y, Filtration and adsorption properties of porous calcium alginate membrane for methylene blue removal from water, Chemical Engineering Journal 316 (2017) 623–630.

[14]. Shi C, Lv C, Wu L, Hou X, Porous chitosan/hydroxyapatite composite membrane for dyes static and dynamic removal from aqueous solution, J Hazard Mater 338 (2017) 241–249. [PubMed: 28570878]

[15]. Yagub MT, Sen TK, Afroze S, Ang HM, Dye and its removal from aqueous solution by adsorption: a review, Adv Colloid Interface Sci 209 (2014) 172–184. [PubMed: 24780401]

[16]. Shi B, Guan H, Shangguan L, Wang H, Xia D, Kong X, Huang F, A pillar[5]arene-based 3D network polymer for rapid removal of organic micropollutants from water, Journal of Materials Chemistry A (2017).

[17]. Verma AK, Dash RR, Bhunia P, A review on chemical coagulation/flocculation technologies for removal of colour from textile wastewaters, J Environ Manage 93 (2012) 154–168. [PubMed: 22054582]

[18]. Zhou Z, Kong D, Zhu H, Wang N, Wang Z, Wang Q, Liu W, Li Q, Zhang W, Ren Z, Preparation and adsorption characteristics of an ion-imprinted polymer for fast removal of Ni(II) ions from aqueous solution, J Hazard Mater 341 (2017) 355–364. [PubMed: 28802246]

[19]. Liu S, Mishra SB, Zhang Y, Qi L, Uptake of Hexavalent Chromium in Electroplating Wastewater by Hydrothermally Treated and Functionalized Sand and Its Sustainable Reutilization for Glass Production, ACS Sustainable Chemistry & Engineering 5 (2017) 1509–1516.

[20]. Perez-Page M, Yu E, Li J, Rahman M, Dryden DM, Vidu R, Stroeve P, Template-based syntheses for shape controlled nanostructures, Adv Colloid Interface Sci 234 (2016) 51–79. [PubMed: 27154387]

[21]. Guo Z-Q, Miao N-X, Zhou J-P, Lei Y-X, Hassan QU, Zhou M-M, Novel magnetic semiconductor Na2Fe2Ti6O16: synthesis, double absorption and strong adsorptive ability, J. Mater. Chem. A 5 (2017) 17589–17600.

[22]. Gupta VK, Kumar R, Nayak A, Saleh TA, Barakat MA, Adsorptive removal of dyes from aqueous solution onto carbon nanotubes: a review, Adv Colloid Interface Sci 193-194 (2013) 24–34. [PubMed: 23579224]

[23]. Chowdhury S, Balasubramanian R, Recent advances in the use of graphene-family nanoadsorbents for removal of toxic pollutants from wastewater, Adv Colloid Interface Sci 204 (2014) 35–56. [PubMed: 24412086]

[24]. Santhosh C, Velmurugan V, Jacob G, Jeong SK, Grace AN, Bhatnagar A, Role of nanomaterials in water treatment applications: A review, Chemical Engineering Journal 306 (2016) 1116–1137.

[25]. Zhao J, Wang Z, White JC, Xing B, Graphene in the aquatic environment: adsorption, dispersion, toxicity and transformation, Environ Sci Technol 48 (2014) 9995–10009. [PubMed: 25122195]

[26]. Yan Y, Miao J, Yang Z, Xiao FX, Yang HB, Liu B, Yang Y, Carbon nanotube catalysts: recent advances in synthesis, characterization and applications, Chem Soc Rev 44 (2015) 3295–3346. [PubMed: 25855947]

[27]. Hou D, Qi S, Zhao B, Rigby M, O'Connor D, Incorporating life cycle assessment with health risk assessment to select the 'greenest'cleanup level for Pb contaminated soil, Journal of Cleaner Production 162 (2017) 1157–1168.

[28]. Hou D, Song Y, Zhang J, Hou M, O'Connor D, Harclerode M, Climate change mitigation potential of contaminated land redevelopment: A city-level assessment method, Journal of Cleaner Production (2017).

[29]. Song Y, Hou D, Zhang J, O'Connor D, Li G, Gu Q, Li S, Liu P, Environmental and socio-economic sustainability appraisal of contaminated land remediation strategies: A case study at a mega-site in China, Science of The Total Environment 610 (2018) 391–401. [PubMed: 28806555]

[30]. Hou D, Gu Q, Ma F, O'Connell S, Life cycle assessment comparison of thermal desorption and stabilization/solidification of mercury contaminated soil on agricultural land, Journal of Cleaner Production 139 (2016) 949–956.

[31]. Hou D, Ding Z, Li G, Wu L, Hu P, Guo G, Wang X, Ma Y, O'Connor D, Wang X, A Sustainability Assessment Framework for Agricultural Land Remediation in China, Land Degradation & Development (2017).

[32]. Hou D, Guthrie P, Rigby M, Assessing the trend in sustainable remediation: A questionnaire survey of remediation professionals in various countries, Journal of Environmental Management 184 (2016) 18–26. [PubMed: 27567932]

[33]. Hou D, Divergence in stakeholder perception of sustainable remediation, Sustainability Science 11 (2016) 215–230.

[34]. Singh DK, Verma DK, Singh Y, Hasan SH, Preparation of CuO nanoparticles using Tamarindus indica pulp extract for removal of As(III): Optimization of adsorption process by ANN-GA, Journal of Environmental Chemical Engineering 5 (2017) 1302–1318.

[35]. Saif S, Tahir A, Chen Y, Green Synthesis of Iron Nanoparticles and Their Environmental Applications and Implications, Nanomaterials (Basel) 6 (2016).

[36]. Akhtar MS, Panwar J, Yun Y-S, Biogenic Synthesis of Metallic Nanoparticles by Plant Extracts, ACS Sustainable Chemistry & Engineering 1 (2013) 591–602.

[37]. Muthukumar H, Matheswaran M, Amaranthus spinosusLeaf Extract Mediated FeO Nanoparticles: Physicochemical Traits, Photocatalytic and Antioxidant Activity, ACS Sustainable Chemistry & Engineering 3 (2015) 3149–3156.

[38]. Machado S, Pacheco JG, Nouws HP, Albergaria JT, Delerue-Matos C, Characterization of green zero-valent iron nanoparticles produced with tree leaf extracts, Sci Total Environ 533 (2015) 76–81. [PubMed: 26151651]

[39]. Huang J, Lin L, Sun D, Chen H, Yang D, Li Q, Bio-inspired synthesis of metal nanomaterials and applications, Chem Soc Rev 44 (2015) 6330–6374. [PubMed: 26083903]

[40]. Shankar SS, Ahmad A, Pasricha R, Sastry M, Bioreduction of chloroaurate ions by geranium leaves and its endophytic fungus yields gold nanoparticles of different shapes, Journal of Materials Chemistry 13 (2003) 1822.

[41]. Kuang Y, Wang Q, Chen Z, Megharaj M, Naidu R, Heterogeneous Fenton-like oxidation of monochlorobenzene using green synthesis of iron nanoparticles, J Colloid Interface Sci 410 (2013) 67–73. [PubMed: 24034218]

[42]. Shahwan T, Abu Sirriah S, Nairat M, Boyacı E, Eroğlu AE, Scott TB, Hallam KR, Green synthesis of iron nanoparticles and their application as a Fenton-like catalyst for the degradation of aqueous cationic and anionic dyes, Chemical Engineering Journal 172 (2011) 258–266.

[43]. Hoag GE, Collins JB, Holcomb JL, Hoag JR, Nadagouda MN, Varma RS, Degradation of bromothymol blue by 'greener' nano-scale zero-valent iron synthesized using tea polyphenols, Journal of Materials Chemistry 19 (2009) 8671.

[44]. Makarov VV, Makarova SS, Love AJ, Sinitsyna OV, Dudnik AO, Yaminsky IV, Taliansky ME, Kalinina NO, Biosynthesis of stable iron oxide nanoparticles in aqueous extracts of Hordeum vulgare and Rumex acetosa plants, Langmuir 30 (2014) 5982–5988. [PubMed: 24784347]

[45]. Saif S, Tahir A, Asim T, Chen Y, Plant Mediated Green Synthesis of CuO Nanoparticles: Comparison of Toxicity of Engineered and Plant Mediated CuO Nanoparticles towards Daphnia magna, Nanomaterials (Basel) 6 (2016).

[46]. Sanchez-Botero L, Herrera AP, Hinestroza JP, Oriented Growth of alpha-MnO(2) Nanorods Using Natural Extracts from Grape Stems and Apple Peels, Nanomaterials (Basel) 7 (2017).

[47]. Ahmed S, Annu SA Chaudhry, S. Ikram, A review on biogenic synthesis of ZnO nanoparticles using plant extracts and microbes: A prospect towards green chemistry, J Photochem Photobiol B 166 (2017) 272–284. [PubMed: 28013182]

[48]. Ismail E, Khenfouch M, Dhlamini M, Dube S, Maaza M, Green palladium and palladium oxide nanoparticles synthesized via Aspalathus linearis natural extract, Journal of Alloys and Compounds 695 (2017) 3632–3638.

[49]. Varma RS, Journey on greener pathways: from the use of alternate energy inputs and benign reaction media to sustainable applications of nano-catalysts in synthesis and environmental remediation, Green Chemistry 16 (2014) 2027.

[50]. Varma RS, Greener approach to nanomaterials and their sustainable applications, Current Opinion in Chemical Engineering 1 (2012) 123–128.

[51]. Sarmah K, Pratihar S, Synthesis, Characterization, and Photocatalytic Application of Iron Oxalate Capped Fe, Fe–Cu, Fe–Co, and Fe–Mn Oxide Nanomaterial, ACS Sustainable Chemistry & Engineering 5 (2017) 310–324.

[52]. Yu M, Han Y, Li J, Wang L, CO 2 -activated porous carbon derived from cattail biomass for removal of malachite green dye and application as supercapacitors, Chemical Engineering Journal 317 (2017) 493–502.

[53]. Li X, Zhang Y, Jing L, He X, Novel N-doped CNTs stabilized Cu 2 O nanoparticles as adsorbent for enhancing removal of Malachite Green and tetrabromobisphenol A, Chemical Engineering Journal 292 (2016) 326–339.

[54]. Lara-Vásquez EJ, Solache-Ríos M, Gutiérrez-Segura E, Malachite green dye behaviors in the presence of biosorbents from maize (Zea mays L.), their Fe-Cu nanoparticles composites and Fe-Cu nanoparticles, Journal of Environmental Chemical Engineering 4 (2016) 1594–1603.

[55]. Das D, Pal A, Adsolubilization phenomenon perceived in chitosan beads leading to a fast and enhanced malachite green removal, Chemical Engineering Journal 290 (2016) 371–380.

[56]. Kan Y, Yue Q, Kong J, Gao B, Li Q, The application of activated carbon produced from waste printed circuit boards (PCBs) by H3PO4 and steam activation for the removal of malachite green, Chemical Engineering Journal 260 (2015) 541–549.

[57]. Zheng Y, Zhu Y, Wang A, Highly efficient and selective adsorption of malachite green onto granular composite hydrogel, Chemical Engineering Journal 257 (2014) 66–73.

[58]. Wei A, Liu B, Zhao H, Chen Y, Wang W, Ma Y, Yang H, Liu S, Synthesis and formation mechanism of flowerlike architectures assembled from ultrathin NiO nanoflakes and their adsorption to malachite green and acid red in water, Chemical Engineering Journal 239 (2014) 141–148.

[59]. Mittal H, Parashar V, Mishra SB, Mishra AK, Fe3O4 MNPs and gum xanthan based hydrogels nanocomposites for the efficient capture of malachite green from aqueous solution, Chemical Engineering Journal 255 (2014) 471–482.

[60]. Jalil AA, Triwahyono S, Yaakob MR, Azmi ZZ, Sapawe N, Kamarudin NH, Setiabudi HD, Jaafar NF, Sidik SM, Adam SH, Hameed BH, Utilization of bivalve shell-treated Zea mays L. (maize) husk leaf as a low-cost biosorbent for enhanced adsorption of malachite green, Bioresour Technol 120 (2012) 218–224. [PubMed: 22820110]

[61]. Zou Y, Liu Y, Wang X, Sheng G, Wang S, Ai Y, Ji Y, Liu Y, Hayat T, Wang X, Glycerol-Modified Binary Layered Double Hydroxide Nanocomposites for Uranium Immobilization via Extended X-ray Absorption Fine Structure Technique and Density Functional Theory Calculation, ACS Sustainable Chemistry & Engineering 5 (2017) 3583–3595.

[62]. Weng X, Guo M, Luo F, Chen Z, One-step green synthesis of bimetallic Fe/Ni nanoparticles by eucalyptus leaf extract: Biomolecules identification, characterization and catalytic activity, Chemical Engineering Journal 308 (2017) 904–911.

[63]. Wang X, Zhan C, Ding Y, Ding B, Xu Y, Liu S, Dong H, Dual-Core Fe2O3@Carbon Structure Derived from Hydrothermal Carbonization of Chitosan as a Highly Efficient Material for Selective Adsorption, ACS Sustainable Chemistry & Engineering 5 (2017) 1457–1467.

[64]. Luo F, Yang D, Chen Z, Megharaj M, Naidu R, The mechanism for degrading Orange II based on adsorption and reduction by ion-based nanoparticles synthesized by grape leaf extract, J Hazard Mater 296 (2015) 37–45. [PubMed: 25910458]

[65]. Wang Z, Fang C, Megharaj M, Characterization of Iron–Polyphenol Nanoparticles Synthesized by Three Plant Extracts and Their Fenton Oxidation of Azo Dye, ACS Sustainable Chemistry & Engineering 2 (2014) 1022–1025.

[66]. Wang Z, Iron Complex Nanoparticles Synthesized by Eucalyptus Leaves, ACS Sustainable Chemistry & Engineering 1 (2013) 1551–1554.

[67]. Kim YK, Kim T, Kim Y, Harbottle D, Lee JW, Highly effective Cs+ removal by turbidity-free potassium copper hexacyanoferrate-immobilized magnetic hydrogels, J Hazard Mater 340 (2017) 130–139. [PubMed: 28715736]

[68]. Cao D, Jin X, Gan L, Wang T, Chen Z, Removal of phosphate using iron oxide nanoparticles synthesized by eucalyptus leaf extract in the presence of CTAB surfactant, Chemosphere 159 (2016) 23–31. [PubMed: 27268791]

[69]. Wang T, Jin X, Chen Z, Megharaj M, Naidu R, Green synthesis of Fe nanoparticles using eucalyptus leaf extracts for treatment of eutrophic wastewater, Sci Total Environ 466-467 (2014) 210–213. [PubMed: 23895784]

[70]. Wei X, Huang T, Yang JH, Zhang N, Wang Y, Zhou ZW, Green synthesis of hybrid graphene oxide/microcrystalline cellulose aerogels and their use as superabsorbents, J Hazard Mater 335 (2017) 28–38. [PubMed: 28414946]

[71]. Liu S, Yao F, Oderinde O, Zhang Z, Fu G, Green synthesis of oriented xanthan gum-graphene oxide hybrid aerogels for water purification, Carbohydr Polym 174 (2017) 392–399. [PubMed: 28821084]

[72]. Wei Y, Fang Z, Zheng L, Tsang EP, Biosynthesized iron nanoparticles in aqueous extracts of Eichhornia crassipes and its mechanism in the hexavalent chromium removal, Applied Surface Science 399 (2017) 322–329.

[73]. Wang X, Wang A, Ma J, Fu M, Facile green synthesis of functional nanoscale zero-valent iron and studies of its activity toward ultrasound-enhanced decolorization of cationic dyes, Chemosphere 166 (2017) 80–88. [PubMed: 27689887]

[74]. Parandhaman T, Pentela N, Ramalingam B, Samanta D, Das SK, Metal Nanoparticle Loaded Magnetic-Chitosan Microsphere: Water Dispersible and Easily Separable Hybrid Metal Nano-biomaterial for Catalytic Applications, ACS Sustainable Chemistry & Engineering 5 (2017) 489–501.

[75]. Gupta K, Khatri OP, Reduced graphene oxide as an effective adsorbent for removal of malachite green dye: Plausible adsorption pathways, J Colloid Interface Sci 501 (2017) 11–21. [PubMed: 28431217]

[76]. Sharma P, Das MR, Removal of a Cationic Dye from Aqueous Solution Using Graphene Oxide Nanosheets: Investigation of Adsorption Parameters, Journal of Chemical & Engineering Data 58 (2013) 151–158.

[77]. Kim H, Watthanaphanit A, Saito N, Simple Solution Plasma Synthesis of Hierarchical Nanoporous MnO2 for Organic Dye Removal, ACS Sustainable Chemistry & Engineering 5 (2017) 5842–5851.

[78]. Vahidhabanu S, Abideen Idowu A, Karuppasamy D, Ramesh Babu B, Vineetha M, Microwave Initiated Facile Formation of Sepiolite-Poly(dimethylsiloxane) Nanohybrid for Effective Removal of Congo Red Dye from Aqueous Solution, ACS Sustainable Chemistry & Engineering (2017).

[79]. Hu J, Deng W, Chen D, Ceria Hollow Spheres As an Adsorbent for Efficient Removal of Acid Dye, ACS Sustainable Chemistry & Engineering 5 (2017) 3570–3582.

[80]. Pei C, Han G, Zhao Y, Zhao H, Liu B, Cheng L, Yang H, Liu S, Superior adsorption performance for triphenylmethane dyes on 3D architectures assembled by ZnO nanosheets as thin as approximately 1.5nm, J Hazard Mater 318 (2016) 732–741. [PubMed: 27493012]

[81]. Zhou J, Lü Q-F, Luo J-J, Efficient removal of organic dyes from aqueous solution by rapid adsorption onto polypyrrole–based composites, Journal of Cleaner Production 167 (2017) 739–748.

[82]. Rajak R, Saraf M, Mohammad A, Mobin SM, Design and construction of a ferrocene based inclined polycatenated Co-MOF for supercapacitor and dye adsorption applications, J. Mater. Chem. A 5 (2017) 17998–18011.

[83]. He S, Zhang F, Cheng S, Wang W, Synthesis of Sodium Acrylate and Acrylamide Copolymer/GO Hydrogels and Their Effective Adsorption for Pb2+and Cd2+, ACS Sustainable Chemistry & Engineering 4 (2016) 3948–3959.

[84]. Reddy DHK, Yun Y-S, Spinel ferrite magnetic adsorbents: Alternative future materials for water purification?, Coordination Chemistry Reviews 315 (2016) 90–111.

[85]. Yao Y, Enhancement of mass transfer by ultrasound: Application to adsorbent regeneration and food drying/dehydration, Ultrason Sonochem 31 (2016) 512–531. [PubMed: 26964979]

[86]. Prasad AS, Iron oxide nanoparticles synthesized by controlled bio-precipitation using leaf extract of Garlic Vine (Mansoa alliacea), Materials Science in Semiconductor Processing 53 (2016) 79–83.

[87]. Hou D, Al-Tabbaa A, Sustainability: A new imperative in contaminated land remediation, Environmental Science and Policy 39 (2014) 25–34.

[88]. Hou D, Al-Tabbaa A, Luo J, Assessing Effects of Site Characteristics on Remediation Secondary Life Cycle Impact with a Generalized Framework, Journal of Environmental Planning and Management 57 (2014).

[89]. Hou D, Al-Tabbaa A, Hellings J, Sustainable site clean-up from megaprojects: lessons from London 2012, Proceedings of the Institution of Civil Engineers-Engineering Sustainability, Thomas Telford Ltd, 2015, pp. 61–70.

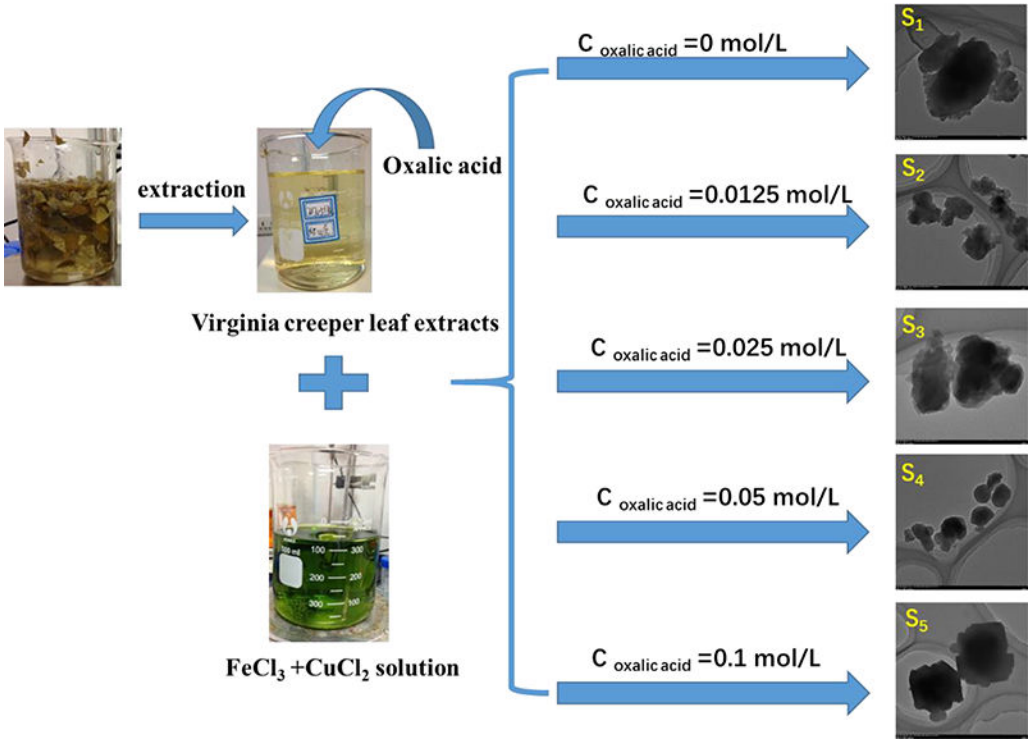

Fig.1.
Schematic illustration of the synthesis of Fe, Cu-based adsorbent

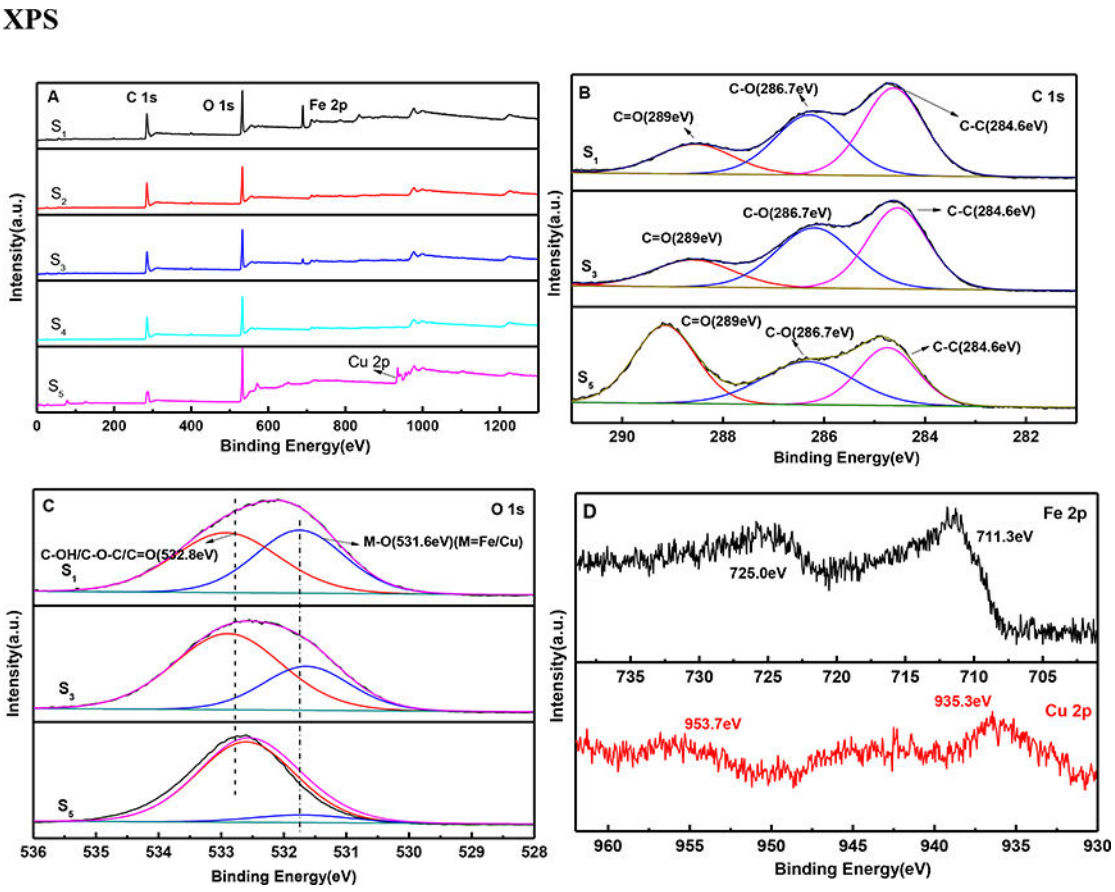

Fig 2.

(A) XPS survey spectrum of S_1-S_5 samples; (B) C 1s spectra of S_1, S_3, and S_5 samples;(C) O 1s spectra of S_1, S_3, and S_5 samples;(D) Fe 2p and Cu 2p spectrum of S_3 sample

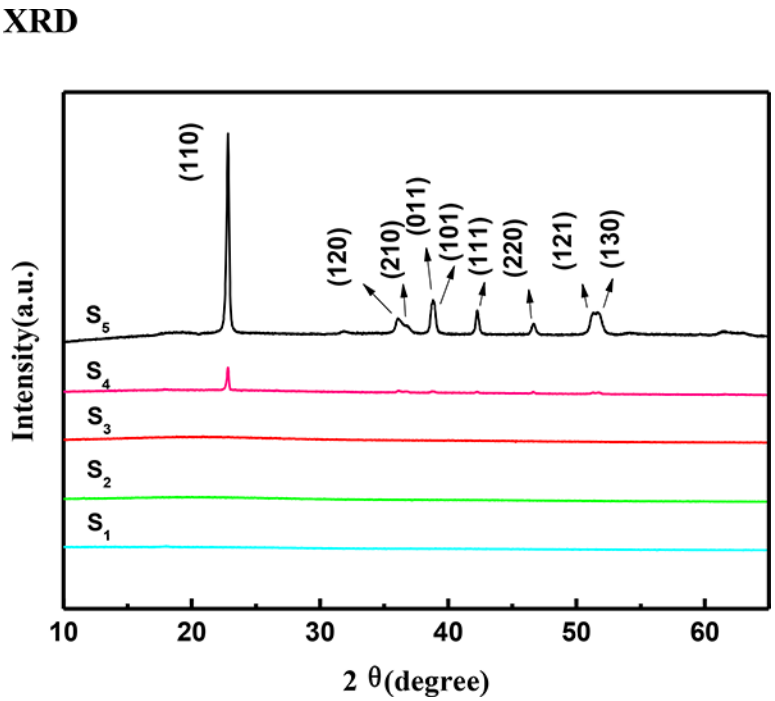

Fig 3.
XRD patterns of the S_1-S_5 samples

FTIR

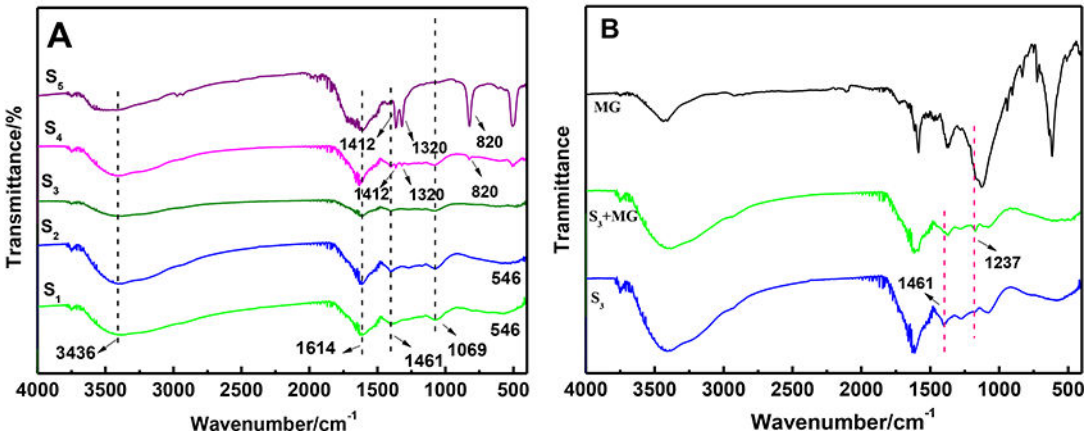

Fig 4.

FTIR spectra for (A) S_1-S_5 samples, (B) MG, S_3 sample before and after adsorption (S_3+MG)

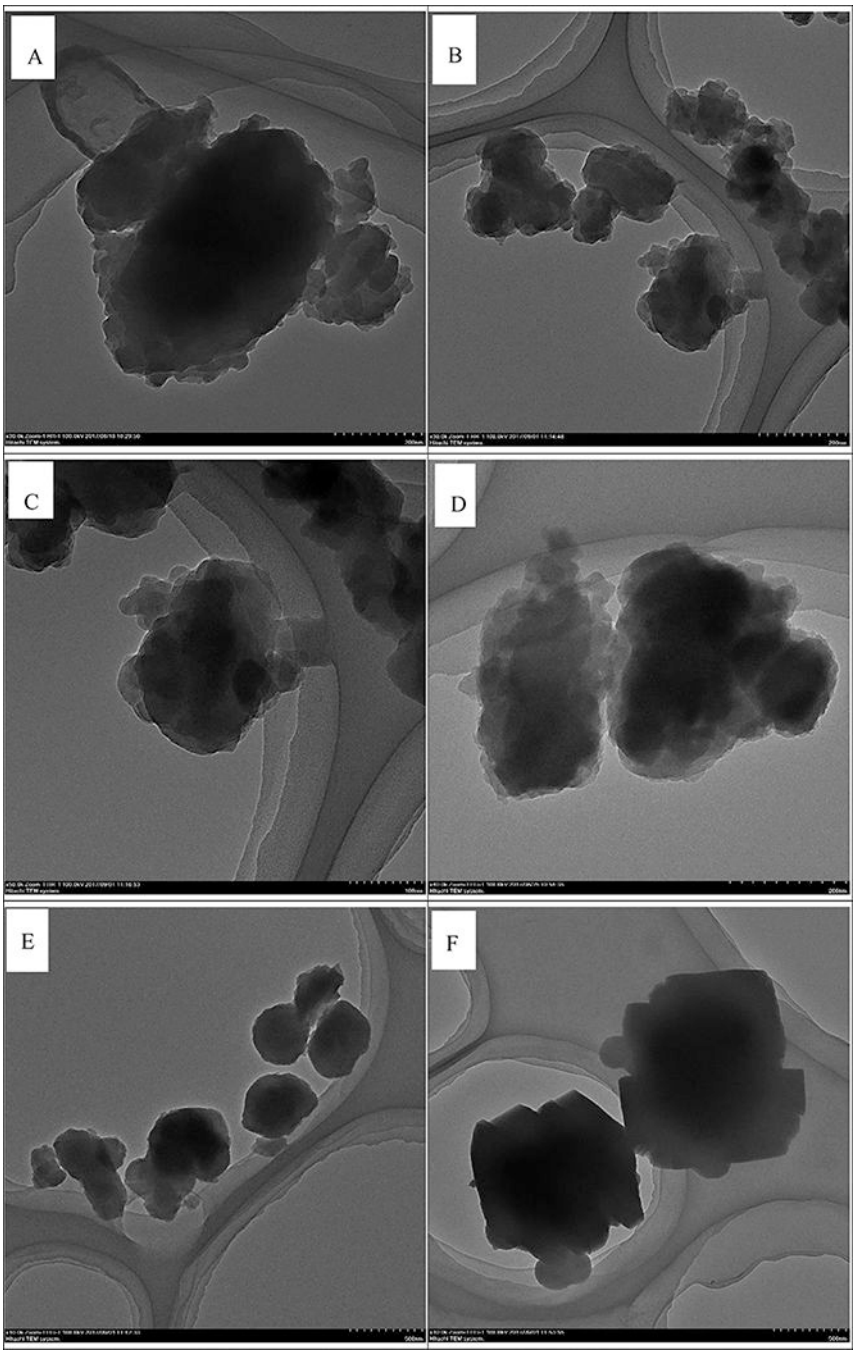

Fig 5.
TEM images of (A) S_1 sample, (B-C) S_2 sample, (D) S_3 sample (E) S_4 sample (F) S_5 sample

BET

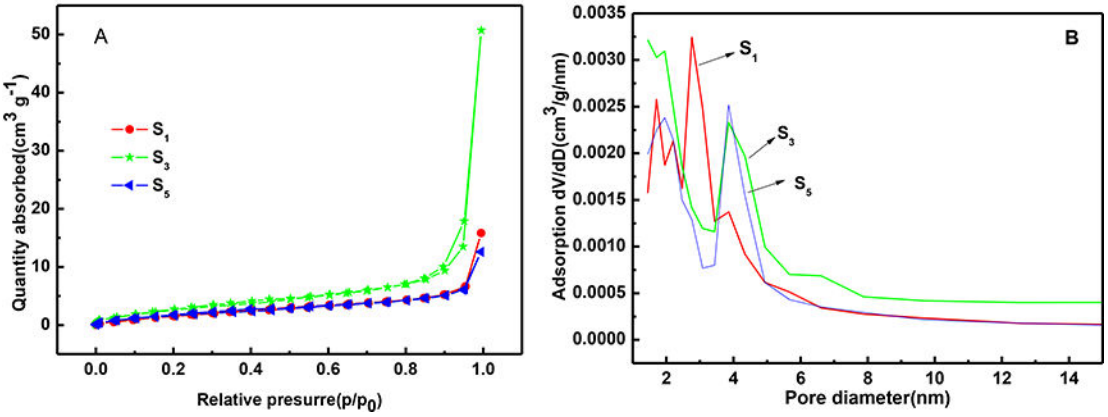

Fig 6.

(A)The nitrogen adsorption-desorption isotherms (B) pore size distributions of the S_1, S_3, and S_5 samples

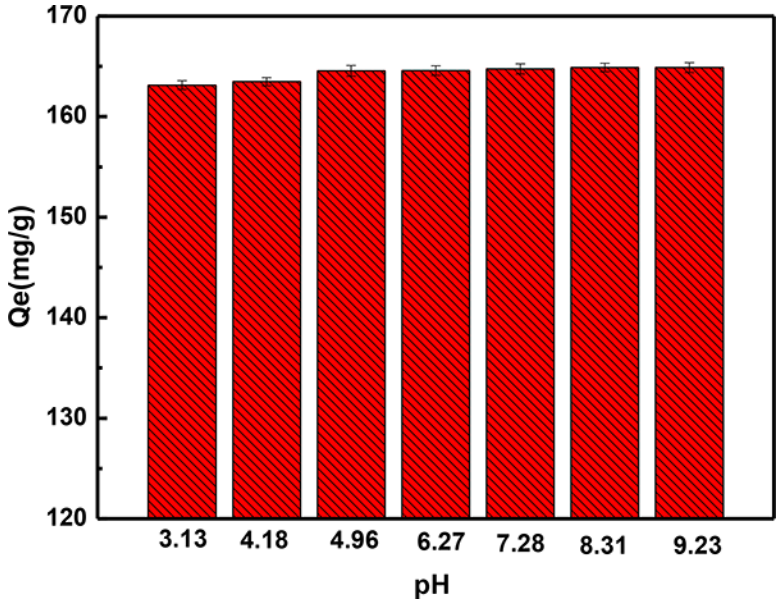

Fig. 7.

The effect of initial pH on the adsorption capacity of S_3 sample. pH = 3.13–9.23; T = 303 K; the amount of adsorbent 0.006 g/20 mL; Initial MG concentration 50 mg/L; contact time = 12 hours.

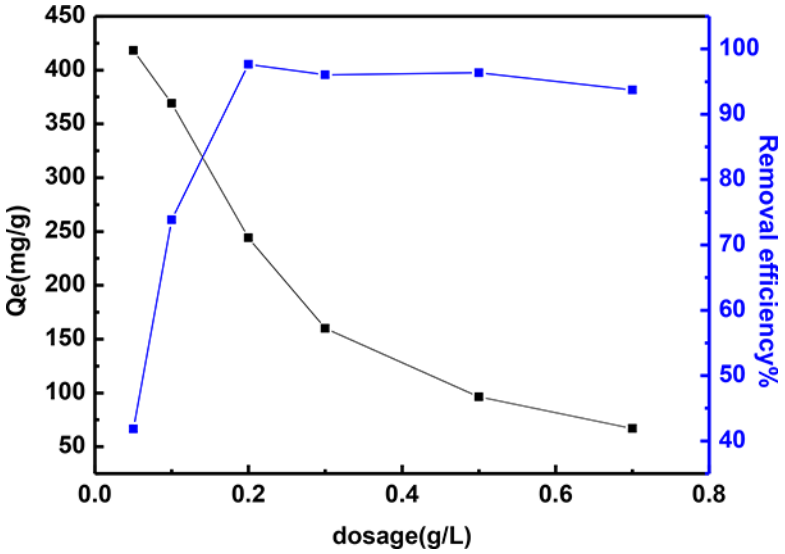

Fig. 8.

The effect of dosage (0.05–0.7 g/L) on the MG adsorption capacity of the S_3 sample. Natural pH of circa 6.6; T = 303 K; Initial MG concentration 50 mg/L; contact time = 12 hours.

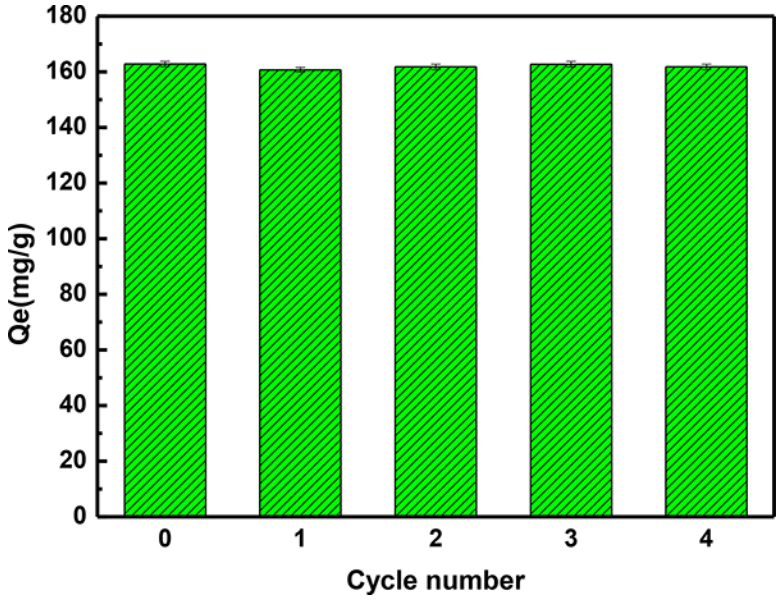

Fig.9.

The MG adsorption capacity of original and regenerated S_3 sample with evolution of adsorption-regeneration cycles. Natural pH of 6.6; temperature 303 K; the amount of adsorbent 0.3 g/L; initial MG concentration 50 mg/L.

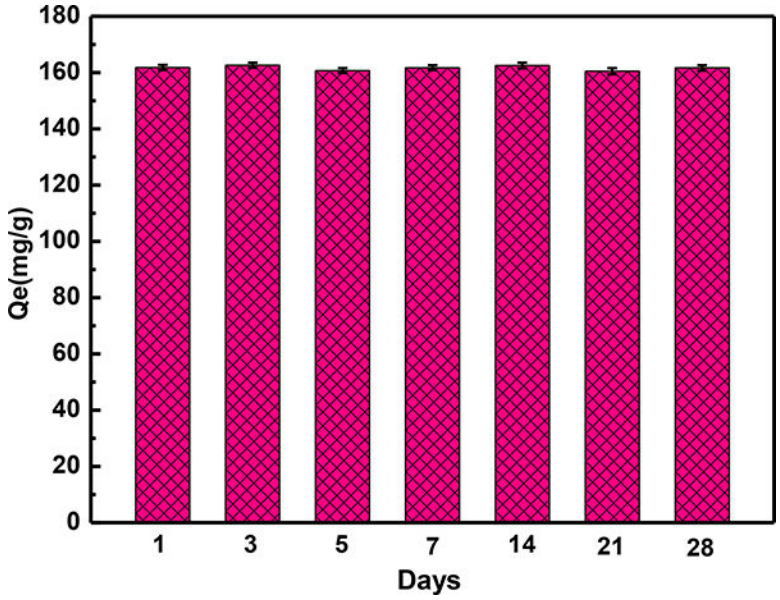

Fig. 10.

The MG adsorption capacity of S_3 sample stored in air for 1,3,5,7,14,21 and 28 days. Natural pH of 6.6; temperature 303 K; the amount of adsorbent 0.3 g/L; initial MG concentration 50 mg/L.

Table 1

Comparison of adsorption capacities of MG adsorbed by various adsorbents.

Adsorbents	Experimental conditions				q_m [c] (mg/g)	References
	Dosage (g/L) [a]	pH	Temp.(K)	C_0 [b] (mg/L)		
CO_2-activated porous carbon	0.4	Undefined	313	40–100	284	[52]
PVP@CNTs-Cu_2O	2.0	Undefined	293	50–3000	1423	[53]
Fe-Cu bagasse composite	1.0	Undefined	298	1–150	61	[54]
chitosan–surfactant–core–shell (CSCS) beads	0.8	7.00	298	10–400	360	[55]
AC-H_3PO_4/Steam	1.0	Undefined	298	500–1200	769	[56]
granular composite hydrogel(AA–IA–APT5)	0.5	Undefined	303	200–1800	2433	[57]
NiO flowerlike nanoarchitectures	0.3	Undefined	Ambient	50	142	[58]
Gx-cl-P(AA-co-AAm)/Fe_3O_4 hydrogel nanocomposite	0.2	neutral pH	298	100–500	497	[59]
bivalve shell-Zea mays L. husk leaf	2.5	6.00	303	10–200	82	[60]
Fe-Cu based adsorbent	0.3	6.58	303	50–500	1399	This work
Fe-Cu based adsorbent	0.3	6.58	313	50–500	1476	This work

a: the mass of the adsorbent contained in each volume of MG aqueous solution

b: the initial concentration of MG in the aqueous solution

c: the maximum adsorption capacity of adsorbent (calculated from the Langmuir model)

Table 2

Kinetic parameters of models for different samples

Samples	$Q_{e,exp}$ (mg/g)	Pseudo-first-order			Pseudo-second-order		
		$Q_{e,1}$	$K_1 \times 10^2$ (min^{-1})	R^2	$Q_{e,2}$	$K_2 \times 10^4$ (g/mg min)	R^2
S_1	110.15	46.31	0.382	0.865	114.28	2.38	0.998
S_2	167.02	50.08	0.394	0.952	172.12	2.46	0.998
S_3	166.57	15.59	0.400	0.955	169.49	8.44	0.999
S_4	164.86	9.090	0.497	0.431	165.84	15.9	0.997
S_5	37.480	27.68	0.304	0.985	42.50	2.63	0.985

Table 3

Isotherm constants and values of R2 for S_3 sample.

T(K)	Langmuir isotherm			Freundlich isotherm			D-R isotherm		
	Q_m(mg /g)	K_L (L/mg)	R^2	K_F (L/g)	n	R^2	Q_m(mg/g)	E(kJ/mol)	R^2
303	1399	0.125	0.996	237	2.389	0.857	980	1.166	0.914
313	1476	0.143	0.998	249	2.254	0.893	942	1.502	0.834
323	1977	0.123	0.990	238	1.603	0.935	967	1.679	0.738

Table 4

Thermodynamics parameters for MG adsorption on the S_3 sample.

Temperature (K)	ΔG0 (kJ mol $^{-1}$)	ΔH0 (kJ mol $^{-1}$)	ΔS0 (J mol $^{-1}$K $^{-1}$)
303	−10.647	25.398	118.96
313	−11.837		
323	−13.026		